The secondary flow and its stability for natural convection in a tall vertical enclosure

By ARNON CHAIT† AND SEPPO A. KORPELA‡

† NASA Lewis Research Center, Cleveland, OH 44135, USA
‡ The Ohio State University, Columbus, OH 43210, USA

The multicellular flow between two vertical parallel plates is numerically simulated using a time-splitting pseudospectral method. The steady flow of air, and the time-periodic flow of oil (Prandtl numbers of 0.71 and 1000, respectively) are investigated and descriptions of these flows using both physical and spectral approaches are presented. The details of the time dependency of the flow and temperature fields of oil are shown, and the dynamics of the process is discussed. The spectral transfer of energy among the axial modes comprising the flow is explored. The spectra of kinetic energy and thermal variance for air are found to be smooth and viscously dominated. Similar spectra for oil are bumpier, and the dynamics of the time-dependent flow are determined to be confined to the lower end of the spectrum alone.

The three-dimensional linear stability of the multicellular flow of air is parametrically studied. The domain of stable two-dimensional cellular motion was found to be constrained by the Eckhaus instability and by two types of monotone instability. The two-dimensional multicellular flow is unstable above a Grashof number of about 8550 (with the critical Grashof number for the base flow being 8037). Therefore the flow of air in a sufficiently tall vertical enclosure should be considered to be three-dimensional for most practical applications.

1. Introduction

The subject matter of this paper is natural convection in a tall vertical enclosure, the convective flow being driven by a temperature difference between isothermal sidewalls. We are only concerned with the limit in which the two aspect ratios of the cavity tend to infinity. In this limit the thermal conditions at the ends are immaterial, for they do not influence the flow in the main part of the cavity. The imposed temperature difference leads to a recirculating flow with upward flow near the hot wall and downward flow next to the cold one. If the temperature differences are small, then the flow away from the ends is a parallel flow, the vertical velocity of which varies as a cubic across the cavity. For such a flow convection heat transfer is absent and temperature across the gap is a linear function of distance. Thus heat is transferred across the enclosure solely by conduction, and for this reason the resulting flow is said to belong to the conduction regime.

By observations and measurements Vest & Arpaci (1969) found that for air the parallel shear flow just described becomes unstable at a Grashof number, Gr, of about 8000, and that the instability sets in as a set of steady two-dimensional cells with axes transverse to the flow direction. Theoretical predictions show this to be true for all fluids for which the Prandtl number, Pr, is less than 12.7 (Gershuni & Zhukhovitskii 1976, p. 276 and Korpela, Gozum & Baxi 1973). Further affirmation of

the instability is given by the interferometric studies of Schinkel (1980) and heat transfer measurements of Hollands & Konicek (1973).

Direct simulations of the multicellular flow after the onset of instability have been carried out, with the aid of a computer, by Lee & Korpela (1983) and Lauriat & Desrayaud (1985 a,b), among others. In their researches the aspect ratio of the cavity was taken to be finite, and their goal was to elucidate the influence of the aspect ratio on the structure of the flow and the resulting heat transfer. Except for the recent study by Nagata & Busse (1983), the only study that takes advantage of the property that in the vertical direction the multicellular flow in a very tall cavity is spatially periodic, is by Gershuni & Zhukhovitskii (1976, pp. 301–304).

One aim of the present work is to study more fully the structure of the multicellular flow by analysing the flow and thermal fields in a typical cell as the nonlinear secondary flow develops. The advantage gained by restricting the analysis to a single cell is high spatial resolution. In addition, because the flow domain is spatially periodic, spectral methods, as opposed to finite-difference or finite-element techniques, may be used for the calculations. This further increases the accuracy of the solutions. The drawback of restricting the domain to one cell is that the wavelength must be prescribed at the outset, and the dependency of the wavelength on the amplitude of convection cannot be established in an infinite domain, even though the correspondence between the two for a given supercritical flow can be found.

A further aim of the present study is to investigate the stability of the multicellular flow. Much of the previous work on stability of secondary flows has been carried out on Rayleigh–Bénard convection and Taylor-Couette flow. The work in convection has been systematically studied by Busse and his coworkers. They have identified a number of secondary instability mechanisms and studied the properties of the stable flows arising from the secondary instability. Some of these instabilities and their main features are summarized in Busse (1981) and in Bolton, Busse & Clever (1986). Briefly, secondary instabilities can be classified according to whether they change only the wavelength of the secondary flow, or whether they change its pattern. Each type of instability is distinguished by its allowable range of wavelengths, its inherent two- or three-dimensionality, its symmetry properties, and its visual appearance in experiments.

The secondary instability for a flow in a vertical cavity has been studied by Nagata & Busse (1983) in the limit of $Pr = 0$. Their results are important for the present study for two reasons. First, our formulation and numerical technique differ from theirs, and therefore our method can be validated by comparing our results at $Pr = 0$ to theirs. Second, their results provide a guide for what can be expected if qualitative similarities exist between the case of a vanishing Prandtl number and one for $Pr = 0.71$, corresponding to air, even if new mechanisms are important for $Pr = 0.71$.

Nagata & Busse found three kinds of instability mechanisms to be present at slightly supercritical Grashof numbers. One kind is the Eckhaus instability (also known as sideband or Benjamin–Feir instability). Its stability boundary defines the domain of the stable two-dimensional convection cells. The second kind is a monotone instability, so called because its most criticial eigenvalue is real. It is responsible for transition to tertiary three-dimensional motion. The third mode is an oscillatory three-dimensional instability. Its critical eigenvalue appears as a complex-conjugate pair, so the flow is a time-dependent tertiary motion of standing waves.
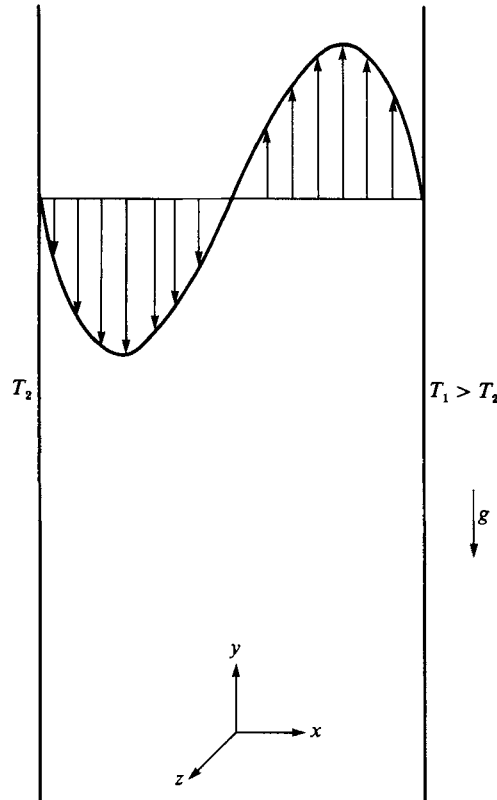
FIGURE 1. Geometry and base velocity profile for an infinite vertical enclosure.

The spatial form of this instability does not lead to a change in the wavelength of the secondary flow.

2. Formulation

The flow in the cavity, (shown in figure 1) with the right wall heated and the left one cooled, is assumed to be governed by the Boussinesq form of the Navier–Stokes equations, which for a two-dimensional flow are

$$\frac{\partial \boldsymbol{v}}{\partial t} = \boldsymbol{v} \times \boldsymbol{\omega} - \boldsymbol{\nabla}\pi + Gr^{-1}(\nabla^2\boldsymbol{v} + T\hat{\boldsymbol{e}}_y), \tag{1}$$

$$\frac{\partial T}{\partial t} = -\boldsymbol{\nabla}\cdot(\boldsymbol{v}T) + (Gr\,Pr)^{-1}\nabla^2 T, \tag{2}$$

$$\boldsymbol{\nabla}\cdot\boldsymbol{v} = 0. \tag{3}$$

The above equations have been put into a non-dimensional form by dividing lengths by the cavity width L, time by $L^2/(Gr\nu)$, temperatures by $\Delta T = T_1 - T_2$, velocities by U and pressure by ρU^2. The characteristic velocity is $U = g\beta\Delta TL^2/\nu$, obtained by balancing the viscous shear force with the buoyant force. In the above definitions β is the volumetric coefficient of thermal expansion, g is the gravitational acceleration

and ν is the kinematic viscosity. The Grashof number is given by $Gr = UL/\nu$, and $Pr = \nu/\kappa$, in which κ is the thermal diffusivity, is the Prandtl number. The vorticity and total head are defined by the equations

$$\boldsymbol{\omega} \equiv \boldsymbol{\nabla} \times \boldsymbol{v}, \tag{4}$$

$$\pi \equiv p + \tfrac{1}{2}\boldsymbol{v}\cdot\boldsymbol{v}. \tag{5}$$

These variables represent total flow quantities. When they are decomposed into a base flow and a secondary flow quantity, the secondary flow variables are designated using a subscript s, and the base flow quantities with a subscript b.

The boundary conditions for the velocities are the no-slip conditions at the walls and periodicity conditions over a cell in the y-direction. The temperature in non-dimensional variables has a value of $-\tfrac{1}{2}$ on the left wall and $\tfrac{1}{2}$ on the right wall.

It turns out to be advantageous to use the secondary flow quantities as the unknowns and decompose the total flow for each of the variables as

$$q(x, y, z, t) = q_s(x, y, z, t) + q_b(x). \tag{6}$$

The base flow is given by the equations

$$v_b = \tfrac{1}{6}(\tfrac{1}{4}x - x^3), \tag{7}$$

$$T_b = x. \tag{8}$$

When the equations governing the base flow are subtracted from the set (1)–(3) one obtains

$$\frac{\partial \boldsymbol{v}_s}{\partial t} = (\boldsymbol{v}_s + \boldsymbol{v}_b) \times (\boldsymbol{\omega}_s + \boldsymbol{\omega}_b) - \boldsymbol{\nabla}\pi_s + Gr^{-1}(\nabla^2 \boldsymbol{v}_s + T_s \hat{\boldsymbol{e}}_y), \tag{9}$$

$$\frac{\partial T_s}{\partial t} = -\boldsymbol{\nabla}\cdot(\boldsymbol{v}_s T_s) + (Gr\,Pr)^{-1}\nabla^2 T_s, \tag{10}$$

$$\boldsymbol{\nabla}\cdot\boldsymbol{v}_s = 0, \tag{11}$$

with homogeneous boundary conditions

$$\boldsymbol{v}_s = T_s = 0 \quad \text{at} \quad x = -\tfrac{1}{2} \text{ and } \tfrac{1}{2}, \tag{12}$$

and periodicity conditions in y. The new pressure head π_s in (9) is now defined by

$$\pi_s \equiv p_s + \tfrac{1}{2}[\boldsymbol{v}_s + \boldsymbol{v}_b(x)]\cdot[\boldsymbol{v}_s + \boldsymbol{v}_b(x)]. \tag{13}$$

3. Numerical method

To resolve the spatial structure of the flow, the set of equations (9)–(12) is solved by a pseudospectral method (Gottlieb & Orszag, 1977) and the evolution of the solution in time is calculated with a three-step time-splitting method. The spectral approximation to the governing equations is obtained by expressing the flow variables as the double sum

$$Q(x, y, t) = \text{Re}\left[\sum_{k=-K+1}^{K} \sum_{n=0}^{N} \hat{Q}(n, k, t)\, T_n(x)\, e^{2\pi i k y/\lambda}\right], \tag{14}$$

in which Re denotes the real part of the expression which follows. This representation uses a spectral sum of Chebyshev polynomials, $T_n(x)$, in x and a Fourier expansion

in y. The parameter λ is the non-dimensional wavelength of the multicellular structure.

The time-splitting method used is due to Marcus (1984a). It is fast and accurate and does not suffer from time-splitting errors. Briefly, the method employs three time steps. In the first step the nonlinear $v \times \omega$ term and the buoyant term in (9) are used to advance the solution in time by an explicit Adams–Bashforth differencing. The second step gives the contribution of the pressure and it is solved implicitly by imposing the continuity equation (11) at this stage. In the last step the influence of the viscous term is taken care of implicitly. A time-splitting error would be introduced in the second step if the boundary conditions were not properly accounted for. Marcus eliminates these errors by introducing a correction which forces the results to satisfy the governing equations and all boundary conditions properly. In addition, he makes efficient use of numerical Green functions (capacitance matrix) in a pre-processing stage and in this way considerably accelerates the computations. Detailed discussion, derivation, and application of the method for circular Couette flow can be found in the original papers of Marcus (1984a, b). The thermal energy balance is advanced in time in two steps. The first is an Adams–Bashforth step which accounts for the nonlinear convective terms. This is followed by an implicit step for the diffusion term.

As this study involves details of the first and second bifurcations of the base flow, numerical accuracy is of great importance. The following section lists several numerical tests which are an integral part of the analysis.

The computer program written for the purpose of simulating the flow was tested by calculating the decay and growth rates of small disturbances in subcritical or slightly supercritical flows, respectively. In addition, for the conditions in which the instability sets in as a travelling wave, the wave speed was determined. The results so obtained were compared with those separately calculated by linear stability theory. A description of how the linear stability problem of the base flow is solved in a similar problem by pseudospectral techniques is given in Kuo (1986). For time steps typical for our study (~ 0.1), the errors in both growth rates and wave speeds were less than 0.1 % with 17 modes in x. The errors become still smaller when more terms in x and smaller time steps are used.

To verify that the nonlinear terms are accurately calculated the normalized divergence of the velocity was computed. It was found to be always $o(10^{-5})$ at each collocation point with 17×16 modes in x and y, respectively, and $o(10^{-9})$ for 33×32 modes. By taking the curl of the Navier–Stokes equations the normalized quantity Y, defined similarly to Marcus (1984a) as

$$Y \equiv \nabla \times [-(v_s \cdot \nabla) v_s + Gr^{-1}(\nabla^2 v_s + T_s \hat{e}_y)], \tag{15}$$

should approach zero at steady state. It was calculated to be less than $o(10^{-6})$ when steady state was reached.

Another test for consistency is to calculate the heat transfer across each vertical plane passing through every horizontal collocation point. At steady state the heat transferred through the walls by conduction alone must be equal to the sum of the conduction and convection at each vertical plane specified by the collocation points. Expressed as an averaged Nusselt number the heat transfer is

$$\overline{Nu} = \frac{1}{\lambda} \int_0^\lambda \left[\frac{\partial T}{\partial x} - Gr\, Pr(uT) \right] dy, \tag{16}$$

where $\overline{Nu} = 1$ for the pure conduction. The steady state was determined to have been reached when the fractional kinetic energy between two time steps changes by less than 10^{-8}. At this condition the maximum deviation in $\overline{Nu}$ among all vertical planes (for 33 collocation points in x) is less than 10^{-6}.

A sensitive test for the overall accuracy is to compute the integrated kinetic energy production and dissipation in the secondary flow. The kinetic energy balance is given by

$$\int_{-0.5}^{0.5} \int_0^\lambda \frac{\partial}{\partial t} (\tfrac{1}{2}u_s^2 + \tfrac{1}{2}v_s^2)\, dy\, dx = -\int_{-0.5}^{0.5} \int_0^\lambda u_s v_s \left(\frac{dv_b}{dx}\right) dy\, dx + Gr^{-1} \int_{-0.5}^{0.5} \int_0^\lambda v_s T_s\, dy\, dx$$

$$- Gr^{-1} \int_{-0.5}^{0.5} \int_0^\lambda \left[\left(\frac{\partial u_s}{\partial x}\right)^2 + \left(\frac{\partial u_s}{\partial y}\right)^2 + \left(\frac{\partial v_s}{\partial x}\right)^2 + \left(\frac{\partial v_s}{\partial y}\right)^2\right] dy\, dx. \quad (17)$$

The first term on the right-hand side of this equation represents energy transfer from the mean flow by the action of Reynolds stress; the second term is the work done by buoyant forces and, if positive, serves also to increase the kinetic energy. The third term is the negative definite viscous dissipation.

The equation for the variance of the temperature is similarly expressed as

$$\int_{-0.5}^{0.5} \int_0^\lambda \frac{1}{2}\frac{\partial T_s^2}{\partial t}\, dy\, dx = -\int_{-0.5}^{0.5} \int_0^\lambda u_s T_s \left(\frac{dT_b}{dx}\right) dy\, dx$$

$$- (Gr\,Pr)^{-1} \int_{-0.5}^{0.5} \int_0^\lambda \left[\left(\frac{\partial T_s}{\partial x}\right)^2 + \left(\frac{\partial T_s}{\partial y}\right)^2\right] dy\, dx. \quad (18)$$

The first term on the right represents the temperature variance created by the interaction of the mean temperature gradient with the convective heat transfer. The second term accounts for the effect of diffusion in smoothing out temperature distortions.

At steady state, production and dissipation of kinetic energy and thermal variance must be equal. Using the same steady state criterion as above and 33×32 modes to resolve the flow, the difference between the production and dissipation was always at most of $O(10^{-7})$ in each of the equations.

4. Simulations of the secondary flow

In this section the flow and thermal structure of two states are presented. The states are representative of slightly and moderately supercritical flows for small and large Prandtl number. The parameters for the first state are $Pr = 0.71$ (air), $Gr = 8500$ (the critical Grashof number being, $Gr_c = 8037$), and $\alpha = 2.8$, where $\alpha = 2\pi/\lambda$ is the wavenumber of a multicellular flow. The second state is for an oil with $Pr = 1000$, $Gr = 375$ ($Gr_c = 276$), and $\alpha = 2.4$. The flow in this state is characterized by two waves travelling in opposite directions giving rise to a steady periodic flow.

Based on results from the stability analyses of the secondary flow (this is discussed in §5) the state for air was chosen to assure a stable two-dimensional flow at the selected conditions. No stability calculations for the time-periodic flow of the oil have been carried out as a part of this study. The state for it then is a somewhat arbitrarily chosen moderately supercritical state. It is not expected that global results, especially with regard to the Prandtl-number dependency, would be greatly altered if at this state for oil the flow were to turn out to be three-dimensional.

In the following two sections, physical and spectral descriptions of the flow are presented, where the ability to examine the flow from both aspects adds to the understanding of the transport phenomena.

4.1. *Physical description of the flow*

For a low-Prandtl-number fluid the stationary multicellular flow, which results from a shear-type instability of the base velocity profile, is shown in the contour plots in the figure 2. The plots in figures 2(a) and 2(d) correspond to the eigenfunction belonging to the eigenvalue with the largest positive growth rate at this state. Even if this flow cannot be seen in nature, comparing it to a state obtained by solving the nonlinear equations serves to illustrate the differences between the two flows. The solid lines in figure 2(a) represent a motion of counterclockwise circulation for which the stream function is positive. The dashed lines represent negative values for the stream function and clockwise rotation. As is evident from figure 2(a), the secondary motion sets in as two stationary counter-rotating cells of the same strength. The cells are inclined with respect to the horizontal in such a way that their upward slope is towards the cold wall.

In figure 2 are also shown the secondary and total fields of the stream function and temperature when the nonlinear terms are retained. Only slight qualitative differences exist between the secondary and the linear fields, because the dominant y-Fourier mode for this slightly supercritical flow is still the first mode. It is also noted that the distinction between the secondary and total fields is appropriate only for an infinitely long cavity. This separation aids in the study of how the non-linear flow develops, but is impossible to perform in a finite domain in a similar manner.

Turning to the flow of a large-Prandtl-number fluid, we note that the instability sets in as two waves travelling in opposite directions in the two halves of the cavity. These waves are the kind that would arise from critical layers. Since the wave speed is greater than the maximum base flow velocity no true critical layers can appear in the flow. This was pointed out by Gill & Davey (1969) who considered the stability of a 'buoyancy layer' (Prandtl 1953), in which the wave speed is also greater than the maximum base flow velocity. They show, as we have also found, that moderately thin layers exist in the flow, in which the conversion of potential energy associated with the buoyancy field to disturbance kinetic energy takes place, and that the kinetic energy of the disturbance is actually slowly transferred to the mean flow rather than vice versa, as is usually the case. These results are consistent also with the findings of Bergholz (1978).

The flow at $Pr = 1000$ is periodic in time. In figure 3 two states are shown at different times during the cyclic variation of the flow. It is noted that, though the secondary fields are shown here, the plots reflect only the fluctuating components of the flow, as the mean flow was found to be identical to the base flow at any instant in time, i.e. the average component of the supercritical flow is identically zero (this is not the case for the flow of air). In the top set of figures (a–d) the kinetic energy reaches its maximum value during the cycle; and on the bottom set of figures (e–h) its minimum. The stream pattern at the maximum of kinetic energy (figure 3a) consists of two counter-rotating convection cells of about equal size and strength. At the minimum of kinetic energy (figure 3e) a weaker and less coherent pattern is shown. The proximity of streamlines in this figure should not be taken as an indication of strong flow, because the maximum value of the stream function is only 0.2×10^{-4}, and the kinetic energy has the value 0.6×10^{-8}. The corresponding numbers for the top figure are 0.2×10^{-3} and 0.1×10^{-6}.
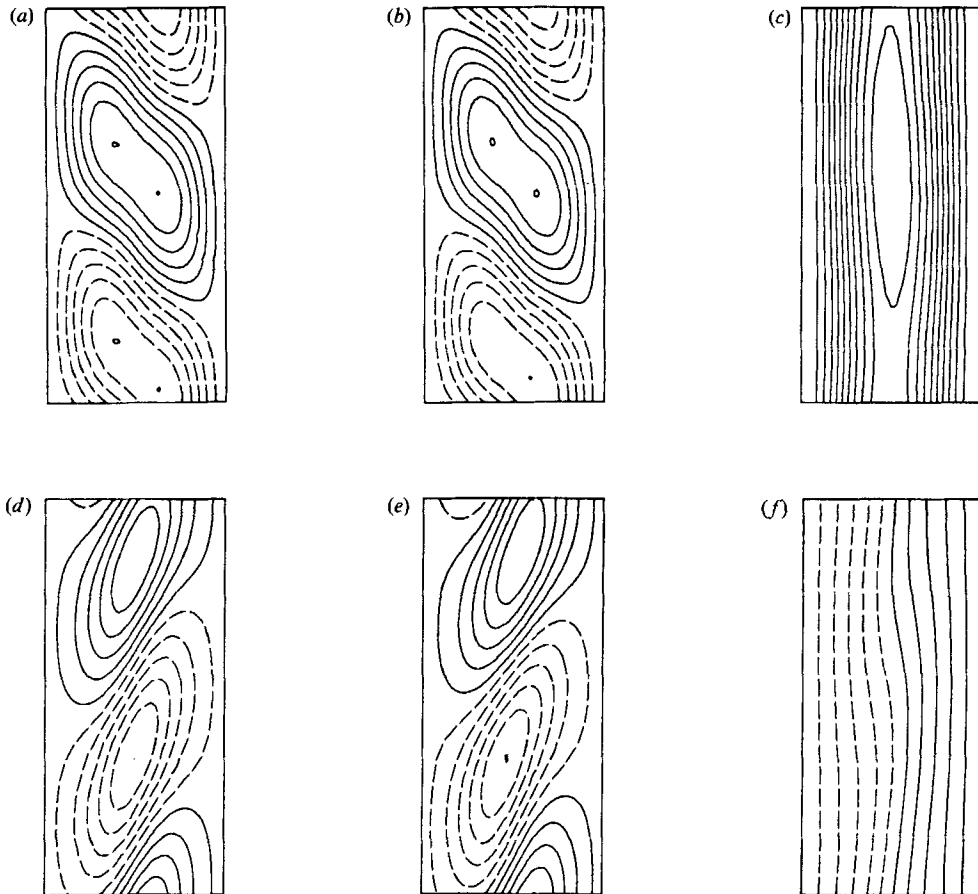
FIGURE 2. The steady flow of air ($Pr = 0.71$, $Gr = 8500$, $\alpha = 2.8$). In each figure the cold wall is on the left and the gravity vector points downwards. (*a*) linear eigenfunction–stream function, (*b*) nonlinear secondary stream function, (*c*) nonlinear total stream function, (*d*) linear eigen-function–temperature, (*e*) nonlinear secondary temperature, (*f*) nonlinear total temperature.

The secondary temperature field, shown in figures 3(*b*) and 3(*f*), is seen to be convected with the travelling waves in such a way that the distinct temperature extrema (of the same sign) are either out of phase (in *b*), or in phase (in *f*). That is, whereas in (*b*) the temperature extrema have opposite signs in a horizontal traverse across the slot, in (*f*) temperature islands of the same sign are side by side. The maximum and minimum of the secondary thermal field are nearly equal in absolute value, both having the value of about 0.1 in the non-dimensional units in which the total temperature difference between the walls is unity. By comparing the stream patterns to the thermal field one notes that strong convection cells correspond to temperature fields that are out of phase, and that weak cellular motion corresponds to thermal fields which are in phase. When the kinetic energy reaches its maximum value, the 'cat's eye' pattern appears in the total flow (figure 3*c*). At the state of minimum kinetic energy the secondary flow is so weak that it has no noticeable influence on the base flow (figure 3*g*).

Figure 4 shows the cyclic variation of both the secondary kinetic energy and the
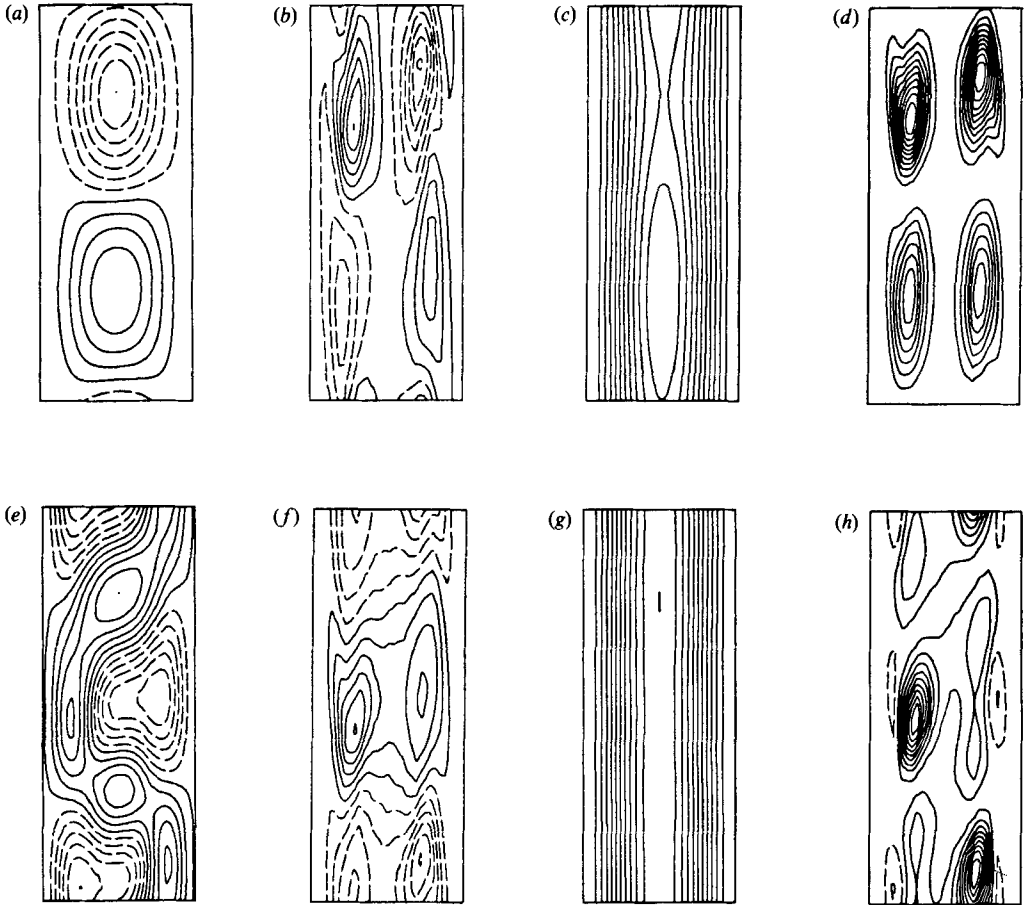
FIGURE 3. The time-periodic flow of oil ($Pr = 1000$, $Gr = 375$, $\alpha = 2.4$). The top figures (a–d) refer to the maximum kinetic energy state and the bottom figures (e–h) to the minimum state. (a,e) secondary stream function, (b,f) secondary temperature, (c,g) total stream function, (d,h) secondary kinetic energy production.

thermal variance. The period is 320 non-dimensional time units (about 4.0 s for, say, engine oil at a mean temperature of 60 °C). As the energy is being transferred to and from the thermal field, the thermal variance cycles in such a way that it is maximum when kinetic energy is minimum and vice versa.

In an attempt to understand why the out of phase thermal fields are conducive for production of secondary kinetic energy and hence strong convection cells, the local production terms in (17) are plotted in figures 3(d) and 3(h). There are two possible sources for the secondary kinetic energy, the first being transfer from the mean flow via Reynolds stresses. For large Prandtl numbers this transfer is insignificant, being only on the order of 10^{-10}. Incidently, it is also negative, so that energy is transferred from the disturbance to the base flow. The dominant production mechanism is the conversion of the potential energy from the buoyancy field, the local production rate being expressed as $v_s T_s$. This term is positive during that part of the cycle in which the thermal fields are out of phase, in the same way as the vertical velocity field is in the two halves of the cavity. This takes place when the streamlines show a
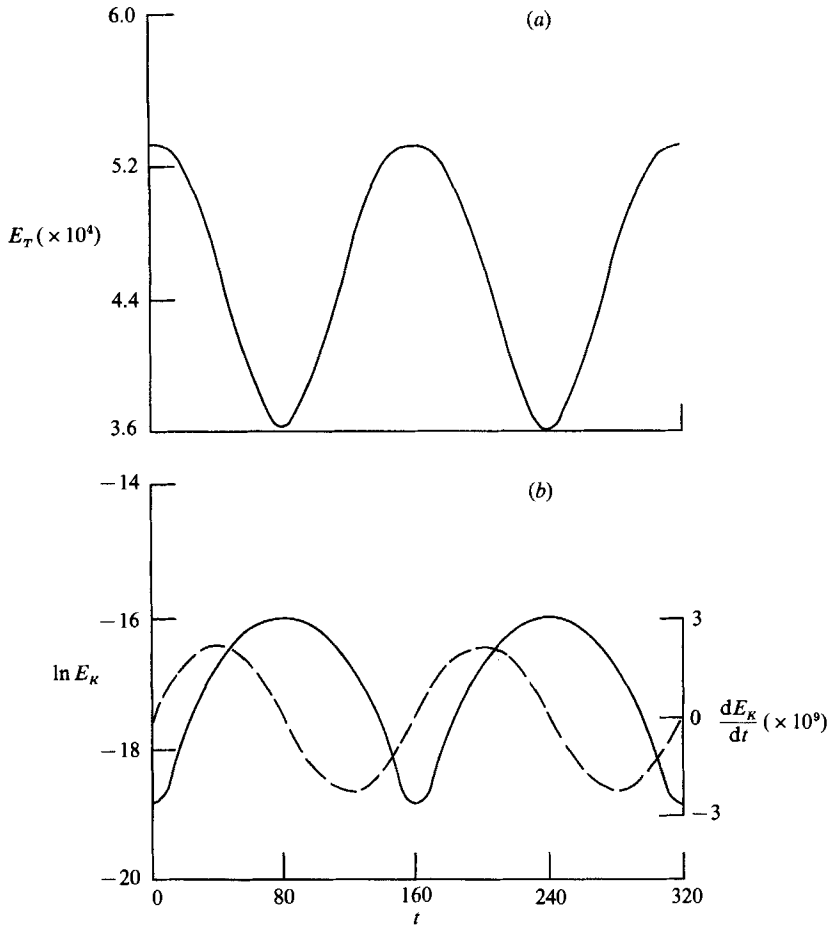
FIGURE 4. Time variations of (a) secondary thermal variance, (b) secondary kinetic energy
(———) and its time derivative (----) ($Pr = 1000$, $Gr = 375$, $\alpha = 2.4$).

regular cellular pattern. The large production rate leads to a maximum of kinetic energy during this part of the cycle. The integrated-value of buoyant production is 0.3×10^{-7}, whereas it is only 0.5×10^{-8} when the thermal fields are in phase.

When inertia and dissipation effects are included, the entire cycle may be described as follows. At the kinetic energy maximum, production is also a maximum owing to the coexistence of both strong production peaks across the cavity, as shown in figure 3(d). However, since the cells are strong, dissipation is also large. Were the production to increase even further, so would the kinetic energy, provided that dissipation is smaller than production. This is not the case though since, as thermal cells of opposite sign start to move away from one another, production begins to decrease. Since dissipation is related to the level of the kinetic energy of the cells (i.e. stronger cells dissipate more than weaker cells), the net balance becomes negative as the kinetic energy maximum is passed. For this reason the kinetic energy begins to decrease. This scenario can also be seen in the switch of the numerical sign of the time rate of change of kinetic energy in figure 4 at the time when the balance between production and dissipation becomes negative.

As the flow in the cells becomes weaker and the thermal islands of opposite sign move further away, the level of buoyant production falls even faster than the

dissipation does, and the rate of the kinetic energy decrease becomes larger. At the point of minimum kinetic energy the cells are so weak that they can no longer span the entire horizontal extent of the cavity, and two weak counter-rotating cells appear in place of each of the strong cells at the kinetic energy maximum (figure 3e). However, at that point thermal cells of opposite sign again start to move towards one another and thereby increase the production term. Again, as dissipation is related to the level of kinetic energy of the flow, it lags behind and a net positive balance is formed when the time rate of change of kinetic energy becomes positive.

In summary, in large-Prandtl-number flows the temperature fluctuations originating near the critical layers are convected in opposite directions on opposite sides of the cavity, and in doing so contribute during part of the cycle to a strong buoyant production of kinetic energy.

The thermal variance changes relatively little in magnitude during the cycle and, as seen from figure 4, it is out of phase with the kinetic energy oscillation. The reason for the small changes is again traced to the passive character of the thermal field for a large-Prandtl-number fluid.

The wave speed for this time-periodic flow is computed to be 7.363. This is slightly lower than the value of 7.585 obtained from the independently performed stability analysis for the same supercritical parameters. Both are somewhat larger than the value 7.202 for the maximum base flow velocity. From previous studies, as well as from our own, we anticipate that linear theory would predict a wave speed of magnitude close to the maximum base flow velocity. What is noteworthy is that the linear and nonlinear values are so close.

4.2. *Spectral description of the flow*

The secondary flow field originates from an instability of a single spectral mode with a given periodicity in the y-direction. The higher harmonics gradually receive energy through nonlinear interactions and the nonlinear states of the flow can be considered to be a synthesis of the various spectral modes. To understand the dynamics of the spectrum one can compute the spectral balance equations for the kinetic energy (E_K) and thermal variance (E_T) and examine the contributions of the various terms in these equations. In doing so it is important to remember that the flow being analysed here is a laminar flow. Thus, whereas the terminology is similar to that used in turbulence research, the modes are not to be regarded as physical eddies. Rather, they are modes defined by the one-dimensional spectra of a two-dimensional flow.

The kinetic energy of the mode with a wavenumber k (the k-mode for short) is defined by

$$E_K(k) \equiv \frac{1}{(1+\delta_{0k})} \int_{-0.5}^{0.5} dx \frac{1}{\lambda^2} \left| \int_0^{\lambda} v(x,y,) e^{-2\pi i k y/\lambda} dy \right|^2 = \frac{1}{(1+\delta_{0k})} \int_{-0.5}^{0.5} |v(x,k)|^2 dx.$$
(19)

where δ_{0k} is the Kronecker delta. That is, the magnitude of the Fourier coefficient of the velocity gives a measure of the spectra kinetic energy. Similarly, thermal variance of the k-mode is defined by

$$E_T(k) \equiv \frac{1}{(1+\delta_{0k})} \int_{-0.5}^{0.5} |T(x,k)|^2 dx.$$
(20)

The evolution equation for the kinetic energy of the k-mode is obtained by a finite Fourier transform of the Navier–Stokes equation and taking the inner product between the transformed equation and the complex conjugate of the transformed

velocity. Integrating the resulting equation across the flow field yields equations for the total and secondary fields, respectively;

$$
\frac{\mathrm{d}E_K(k)}{\mathrm{d}t} = \frac{1}{(1+\delta_{0k})} \Bigg[\mathrm{Re} \Bigg\{ -\int_{-0.5}^{0.5} \sum_{k'=-\infty}^{\infty} [\{v(x, k-k') \cdot \boldsymbol{\nabla}\} v(x, k')] \cdot v(x, -k) \, \mathrm{d}x
$$

$$
-\frac{1}{Gr} \int_{-0.5}^{0.5} v(x, -k) \, T(x, k) \, \mathrm{d}x \Bigg\}
$$

$$
-\frac{1}{Gr} \int_{-0.5}^{0.5} \left(\left| \frac{\partial u(x, k)}{\partial x} \right|^2 + \left| \frac{\partial v(x, k)}{\partial x} \right|^2 + k^2 \, | \, u(x, k) \, |^2 + k^2 \, | \, v(x, k) \, |^2 \right) \mathrm{d}x \Bigg], \quad (21)
$$

$$
\frac{\mathrm{d}E_{Ks}(k)}{\mathrm{d}t} = \frac{1}{(1+\delta_{0k})} \Bigg[\mathrm{Re} \Bigg\{ -\int_{-0.5}^{0.5} \sum_{k'=-\infty}^{\infty} [\{v_s(x, k-k') \cdot \boldsymbol{\nabla}\} v_s(x, k')] \cdot v_s(x, -k) \, \mathrm{d}x
$$

$$
-\int_{-0.5}^{0.5} u_s(x, k) \, v_s(x, -k) \frac{\mathrm{d}v_b}{\mathrm{d}x} \, \mathrm{d}x - \frac{1}{Gr} \int_{-0.5}^{0.5} v_s(x, -k) \, T_s(x, k) \, \mathrm{d}x \Bigg\}
$$

$$
-\frac{1}{Gr} \int_{-0.5}^{0.5} \left(\left| \frac{\partial u_s(x, k)}{\partial x} \right|^2 + \left| \frac{\partial v_s(x, k)}{\partial x} \right|^2 + k^2 \, | \, u_s(x, k) \, |^2 + k^2 \, | \, v_s(x, k) \, |^2 \right) \mathrm{d}x \Bigg]. \quad (22)
$$

The first term on the right in both equations is a spectral convolution sum over all k' modes, and is the result of a nonlinear triad intereaction in which energy is being transferred among modes with harmonic numbers k', $\mp k-k'$, $\pm k$. The second term in (22) represents a direct transfer of energy from the base flow into the k-mode by the action of Reynolds stresses or vice versa. This term is absent in the balance of kinetic energy for the total flow. The next term in both equations is the buoyant conversion term, in which the k-mode either receives energy directly from the thermal field or gives it up. The last term is a negative definite dissipation term.

The appearance of the buoyant conversion term in the equation has consequences for the overall structure of the E_K and the E_T spectra. This term is absent in isothermal flows, or in a convective flow of vanishing Prandtl number. In such cases the only mechanism for energy transfer to the higher modes is through the triad term. With the buoyant term present higher modes can also be supplied energy directly from the thermal field.

The thermal variance equation for the k-mode is obtained similarly by first taking the finite Fourier transform of the thermal energy balance and then multiplying it by the complex conjugate of the temperature of the k-mode. After integration in x the resulting equation is for the total and secondary fields, respectively:

$$
\frac{\mathrm{d}E_T(k)}{\mathrm{d}t} = \frac{1}{(1+\delta_{0k})} \Bigg[\mathrm{Re} \Bigg\{ -\int_{-0.5}^{0.5} \sum_{k'=-\infty}^{\infty} [v(x, k-k') \cdot \boldsymbol{\nabla} T(x, k')] \, T(x, -k) \, \mathrm{d}x \Bigg\}
$$

$$
+ \delta_{0k} \frac{\partial T}{\partial x} (x = \pm 0.5, k) - \frac{1}{Ra} \int_{-0.5}^{0.5} \left\{ \left| \frac{\partial T(x, k)}{\partial x} \right|^2 + k^2 \, | \, T(x, k) \, |^2 \right\} \mathrm{d}x \Bigg], \quad (23)
$$

$$
\frac{\mathrm{d}E_{Ts}(k)}{\mathrm{d}t} = \frac{1}{(1+\delta_{0k})} \Bigg[\mathrm{Re} \Bigg\{ -\int_{-0.5}^{0.5} \sum_{k'=-\infty}^{\infty} [v_s(x, k-k') \cdot \boldsymbol{\nabla} T_s(x, k')] \, T_s(x, -k) \, \mathrm{d}x
$$

$$
-\int_{-0.5}^{0.5} u_s(x, k) \, T_s(x, -k) \frac{\mathrm{d}T_b}{\mathrm{d}x} \, \mathrm{d}x \Bigg\}
$$

$$
-\frac{1}{Ra} \int_{-0.5}^{0.5} \left\{ \left| \frac{\partial T_s(x, k)}{\partial x} \right|^2 + k^2 \, | \, T_s(x, k) \, |^2 \right\} \mathrm{d}x \Bigg]. \quad (24)
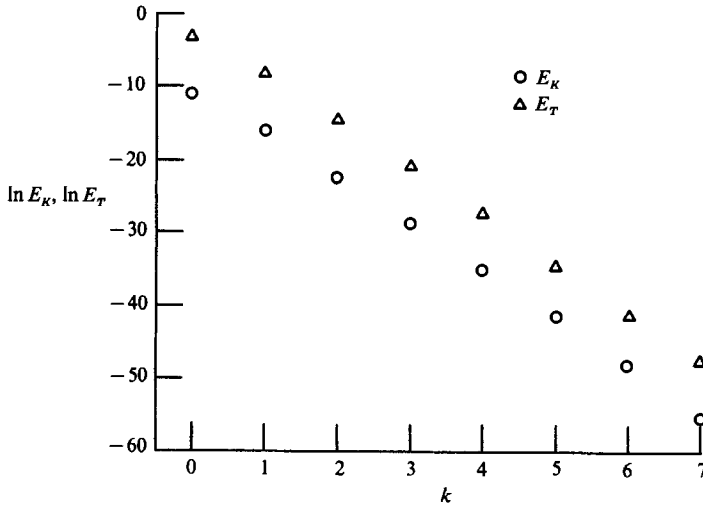$$

FIGURE 5. Spectra of kinetic energy and thermal variance for air ($Pr = 0.71$, $Gr = 8500$, $\alpha = 2.8$).

The first term on the right in both equations is a nonlinear triad interaction. The second term in (24) represents thermal variance production via the interaction of the convective flux of the k-mode with the base temperature gradient. For the total thermal variance equation this term is absent and is replaced by the production of the mean thermal variance at the side-walls. The third term in both equations is the negative definite dissipation of thermal variance by conduction.

4.2.1. *Multicellular flow of air, $Pr = 0.71$*

Figure 5 shows the E_K and E_T spectra for air for a stable, two-dimensional, slightly supercritical state. Both spectra are relatively smooth and they can reasonably be approximated by

$$\ln [E_K(k), E_T(k)] \sim -2\beta k. \tag{25}$$

By fitting a line through the discrete spectra, the resulting value of β at this state is 3.2. A similar calculation made at $Gr = 12000$ yields a value 1.79. Thus the slopes in figure 5 are milder for more supercritical flows. This is caused by the greater effectiveness of the triad transfer mechanism at the larger values of Gr. Based on these and two other calculations β appears to scale as.

$$\beta \sim (Gr - Gr_c)^{\frac{1}{4}}. \tag{26}$$

Marcus (1984b), whom we follow also in the treatment of the spectra, has shown that the relation implied in (25) is consistent with the Navier–Stokes equation for Taylor–Couette flow, and he proposed that the reason the E_K spectrum is smooth in a non-convective flow is that all but the largest mode must receive their energy through the nonlinear triad interaction term, and that this term is not associated intrinsically with any particular wavelength. The existence of a direct transfer of energy from the thermal field to a particular mode means that were a good correlation between $v(x, -k)$ and $T(x, k)$ to exist, a bump would appear in the spectrum. For this reason the E_K spectra of convective flows might not be smooth.

The expected behaviour of the E_K spectrum for our convective flow is not present in the spectrum shown in figure 5. The direct transfer from the thermal field is weak

and modes other than the first two dissipate more energy than they produce. The balance is brought in by the triad term, which dominates the spectrum for $k > 1$. The dominance of the triad interactions leads to a smooth E_K spectrum and therefore for $k > 1$ the spectrum shows no distinct structure.

To make these remarks plausible we define, in a manner similar to Marcus (1984*b*) for Taylor–Couette flow, a local Kolmogorov wave number k_K, in such a way that the local Grashof number based on k_K is unity. The spectrum for wavenumbers larger than k_K should then be dissipative. The Grashof number, using a characteristic scalar velocity $v(k_K)$, then becomes

$$\frac{v(k_K)\,\lambda_k}{\nu} \equiv 1. \tag{27}$$

The wavelength $\lambda_k = \lambda/k_K$ corresponds to the Kolmogorov wavenumber k_K, and $v(k_K)$ and λ are dimensional quantities at present. The characteristic scale velocity $v(k)$ can be defined in terms of the kinetic energy, $E_K(k)$ as

$$v(k) \equiv [E_K(k)]^{\frac{1}{2}}, \tag{28}$$

which when substituted into (27) and the result put into a non-dimensional form gives the relation

$$\frac{E_K(k_K)}{k_K^2} = \frac{1}{\lambda^2\,Gr^2}. \tag{29}$$

Using the numerically computed spectrum (with interpolation between the discrete data), the Kolmogorov wavenumber becomes $k_K \approx 1.7$. The spectrum of E_K shown in figure 5 is therefore certainly dissipative for $k \geqslant 2$. As will be shown, the absolute value of the ratio of production to dissipation is largest for $k = 2$ among all modes with $k \geqslant 2$ and its magnitude is only 0.42. The same ratio for the $k = 1$ mode is 1.03. Therefore it is expected from these two values alone that production will equal dissipation somewhere between the two modes. The rest of the production spectrum decreases exponentially as the wavenumber increases. Dissipation is also confined to the mean flow, for it dissipates about 99.07 % of the total.

The E_T spectrum as shown in figure 5 is also smooth and parallel to the E_K spectrum. Again, analysis shows that all modes except $k = 1$ are dissipative, as the ratio of production to dissipation for $k = 1$ is ~ 1.05 whereas for $k = 2$ it is only ~ 0.45, and even smaller for the higher modes. Therefore, the triad term in (23) and (24) dominates the E_T spectrum, and is a cause of smoothness. It will be seen that this will not be true for a large-Prandtl-number flow.

As an additional check on the accuracy of the simulations, the global E_K and E_T balances at steady state were calculated by summing the production and dissipation over all modes. The sum of the triad interaction terms in each equation must vanish because they represent a transfer of either E_K or E_T among all modes. The total production of kinetic energy was computed to be 0.1575747×10^{-6}. The dissipation also equals this value to 7 significant digits. The production and dissipation for E_T were both 0.1686678×10^{-3}. This kind of accuracy gives us confidence that the physical phenomenon is faithfully simulated.

In the examination of the energetics of the linear stability problem, the decomposition of the flow into a base and secondary flow gives the transfer between these fields. For the $k = 0$ mode the transfer from the base flow is zero because the continuity equation requires that $u(x, k = 0) = 0$. The buoyant interaction with the base temperature field and the $k = 0$ mode accounts for about 4 % of the total production in the flow. For the $k = 1$ mode the situation is reversed, with over 91 %

of the total production coming by interaction with the base flow. The buoyant conversion for the $k = 1$ mode is about 5%. In all modes buoyant production is positive, but for modes with $k \geqslant 1$ kinetic energy is actually transferred from the secondary flow into the base flow, in an amount which makes the net production negative for these modes. The transfer from these higher modes is less than 1% of the total production.

When the total fields are discussed in the thermal variance equation, the only production is by the $k = 0$ mode at the side-walls, and by the $k = 1$ mode. The percentages of the total production by the $k = 0$ and 1 modes are more than 99% and less than 2%, respectively. Thermal variance at the higher modes comes strictly from the nonlinear triad term. When examining the secondary fields, the $k = 0$ mode production is always zero because $u(x, k = 0) = 0$. The $k = 1$ mode is the only mode producing in the E_T spectrum. For the remaining modes the remaining terms are actually negative, but their sum is less than 2% of the total production of the thermal variance.

Dissipation, like production, occurs mainly in the first two modes in the total field, especially in the E_K equation. The $k = 0$ and 1 modes account for about 99.08% of the total dissipation for the E_K spectrum. These modes are responsible for over 98% of the E_T dissipation. The reason for the majority of the dissipation being at the low end of the spectrum is that the transfer mechanism in a two-dimensional laminar flow is too weak to allow either kinetic or thermal variance to be transferred into the higher modes at a sufficient rate for these modes to dissipate a significant amount of the energy. Since $\ln E_K \sim -2\beta k$, an estimate for a characteristic velocity is $v \sim e^{-\beta k}$ and the triad term (excluding the contribution of spatial derivatives which vary algebraically at most with k) becomes $\sim e^{-3\beta k}$. This means that the transfer mechanism drops with increasing k at a faster rate than the kinetic energy. As a result, the level of E_K and E_T is so much higher in the lower modes that most of the dissipation must take place there.

The triad transfer terms in (21) and (22) show that the kth mode interacts with two other modes and exchanges energy in the process. When the total energy transfer into each mode from interaction with all other modes is summed over the entire spectrum, it matches the total energy output (to within 10^{-9} of the quantity), as it should, for the triad term only distributes the energy among the modes. A detailed budget for the total flow can now be summarized as follows.

The net transfer via the triad interaction for the mean component of the flow is negative. The same net transfers for all other modes are positive. This means that energy flows from the mean flow into the fluctuating components. Specifically, *all* the energy leaving the $k = 0$ mode goes to the $k = 1$ mode. However, when the mean flow interacts with the $k > 1$ modes, energy is always being transferred from these modes *back* into the mean flow. It is noted that the total amount coming from all the $k > 1$ modes into the $k = 0$ mode is only 0.16% of the amount transferred from the mean flow into the $k = 1$ mode.

Modes with $k > 1$ *receive* most of their energy by interacting with the $k = 1$ and $k - 1$ modes. For $2 \leqslant k \leqslant 7$, such interactions result in transfers of amounts which are larger than 99.9% of the total transfer into each of these modes.

An examination of the fractional energy which *leaves* the kth mode reveals that for $k < 4$ most of the energy goes into the mean flow, at a rate diminishing with increasing k. The fractional values are given in figure 6, which shows that a large portion of the total energy leaving the higher modes is by interaction with the $k = 2$ and 3 modes. In interpreting figure 6, it is important to recall that the E_K
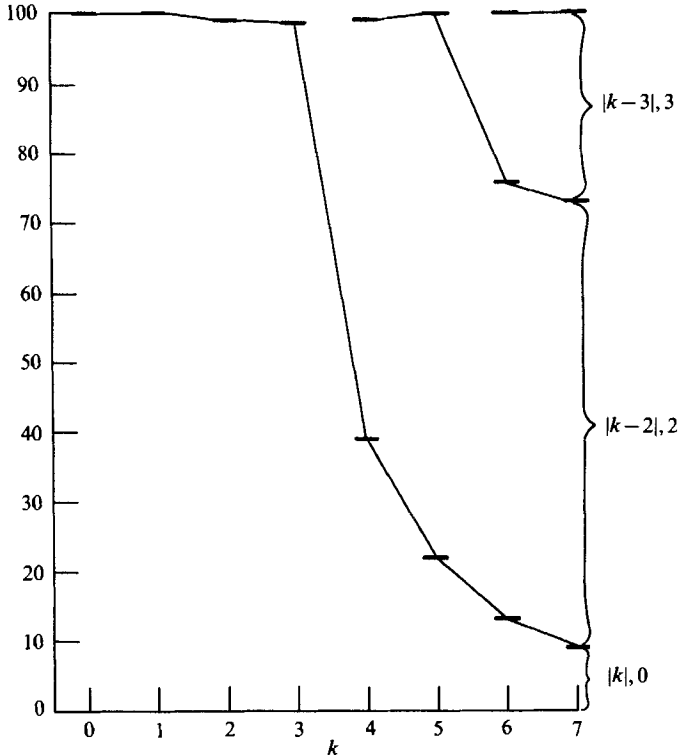
FIGURE 6. Amount of energy transferred from the k-mode into other modes via the triad term, expressed as a percentage of the total energy outflow via the triad term at the k-mode ($Pr = 0.71$, $Gr = 8500$, $\alpha = 2.8$).

spectrum falls exponentially with k. For example, whereas for $k = 2$ and $k = 3$ modes about 98.9% of their energy transfer via the triad interaction goes back into the mean flow, the amount leaving $k = 2$ is about 375 times the amount transferred out of $k = 3$.

Results were also obtained for a pure shear flow ($Pr = 0$) in which the transfer of energy from the buoyant field is by the interaction between the mean flow and the mean temperature field (i.e. production at $k = 0$ mode only). The trends discussed here for the $Pr = 0.71$ case were found to be true for the flow with $Pr = 0$ as well.

Another way to look at the energetics of the flow is to plot the horizontal distribution of the y-averaged production from both the base flow ($\bar{\mathcal{P}}_b$) and the buoyancy field ($\bar{\mathcal{P}}_T$). These are shown in figure 7, together with the dissipation ($\bar{\mathcal{D}}$). Both production mechanisms peak at the centre of the cavity. The energy produced near the centre is transferred towards the wall where a small part of it is drawn into the base flow or stored in the buoyancy field. Most of the dissipation takes place right next to the wall.

4.2.2. *Oscillatory flow for a fluid with* $Pr = 1000$

As has already been mentioned the flow of a fluid with $Pr = 1000$ is periodic in time. The kinetic energy spectra, when the kinetic energy reaches its maximum and minimum, are presented in figure 8. Comparison with figure 5 shows that, for this
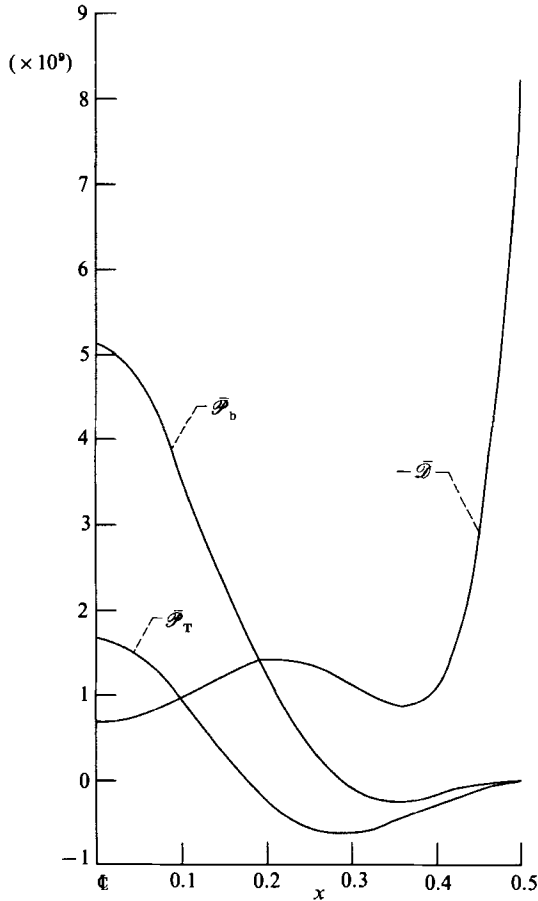
FIGURE 7. Average kinetic energy production and dissipation across the cavity
$(Pr = 0.71, Gr = 8500, \alpha = 2.8)$.

periodic flow, more modes participate in the dynamics at the low end of the spectrum than in the low-Prandtl-number flow, resulting in a non-smooth spectra. The base–secondary flow decomposition shows that production at $Pr = 1000$ is almost solely determined by conversion from the buoyancy field (typical ratios of buoyant production to base flow transfer are $10^2 - 10^3$). As described earlier on physical grounds, it is the horizontal coexistence of two production peaks in the cavity that gives rise to a coherent, large-scale structure at the kinetic energy maximum. As expected, the dominant mode in the spectrum is the $k = 1$ mode which goes through the widest swings in its kinetic energy level. The $k = 2$ mode is almost stationary, and the $k = 3$ mode shows cyclical variations, out of phase with the $k = 1$ variations. It is significant to note that the stream patterns show structure corresponding to $k = 3$ at the cycle minima. Thus, whereas for $Pr = 0.71$ the higher modes serve only to distort the mean flow and the $k = 1$ mode, now the $k = 3$ mode has a clearer physical interpretation. None of the modes above the $k = 3$ mode participate in any significant way in the time evolution of the flow. Therefore the dynamics of the velocity field are determined by the first four modes *alone*. This is not to say that all modes above $k = 3$ could be discarded in a simulation, since doing so would cause
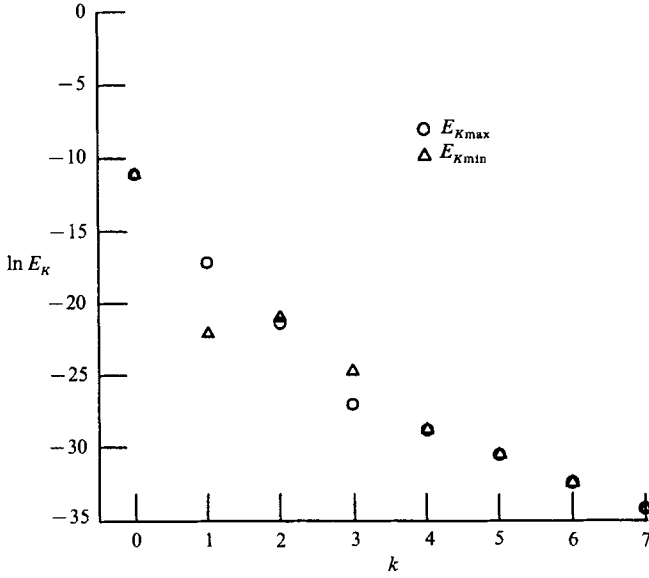
FIGURE 8. Spectra of kinetic energy for oil ($Pr = 1000$, $Gr = 375$, $\alpha = 2.4$).
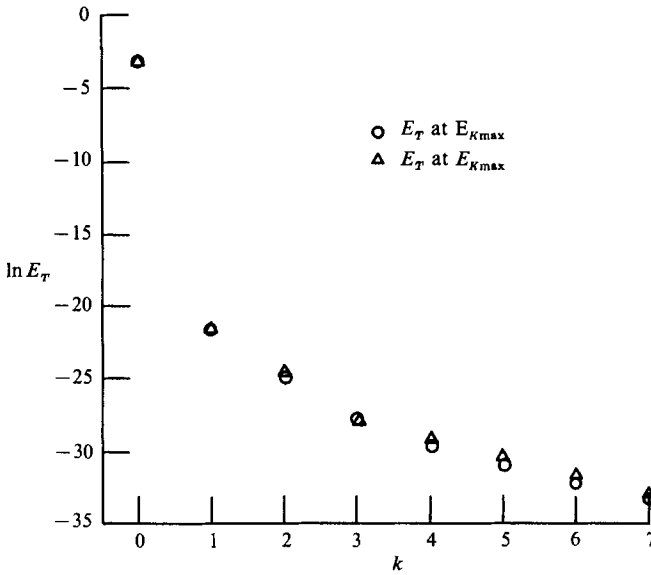

FIGURE 9. Spectra of thermal variance for oil ($Pr = 1000$, $Gr = 375$, $\alpha = 2.4$).

aliasing errors to significantly contaminate the lower modes. The high end of the spectrum shows again an exponential decay which assures that the flow is well resolved.

In figure 9 the spectra of the temperature variance are shown to change very little throughout the cycle. This is consistent with the observation made above about the isotherms in figure 3. During a cycle the secondary temperature cells simply drift up along the hot side and down along the cold side. The variations at $1 \leqslant k \leqslant 4$ change
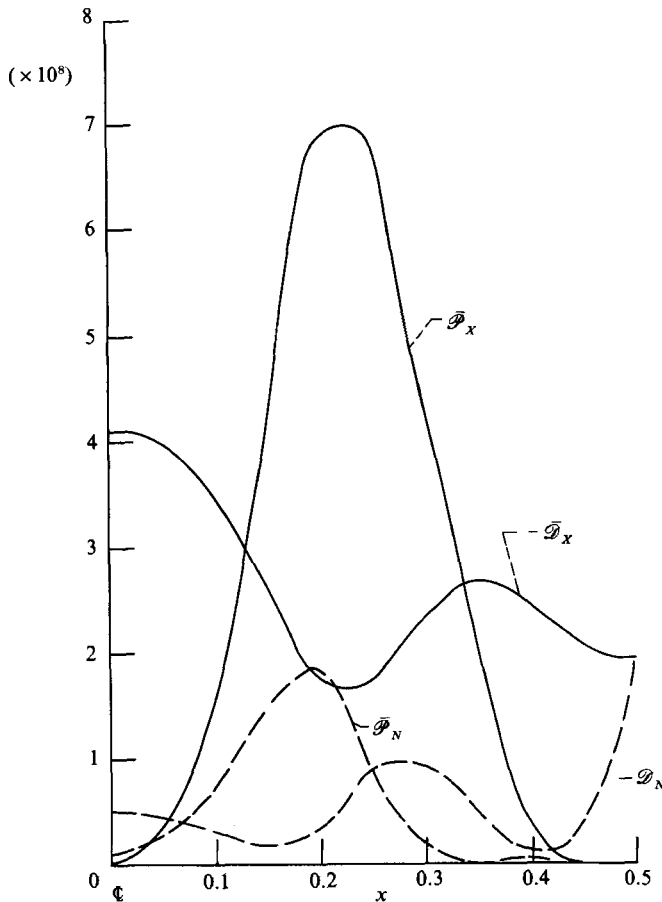
FIGURE 10. Average kinetic energy production and dissipation across the cavity ($Pr = 1000$, $Gr = 375$, $\alpha = 2.4$). $X = E_{k\mathrm{max}}$; $N = E_{k\mathrm{min}}$.

the level of the fluctuating thermal variance by a factor of 1.5, which is small compared with the cyclical changes of order 10^2 in the fluctuating secondary kinetic energy spectra. The high end of the thermal spectrum is again exponentially decaying.

The vertically averaged buoyant production and the dissipation of secondary kinetic energy are shown in figure 10 as a function of the horizontal distance. Production peaks near $x = \pm0.21$. The maximum base flow velocity occurs at $x = \pm0.29$. Interestingly, the vertically averaged dissipation at the kinetic energy maximum peaks not at the walls, but in the interior. At the minimum of kinetic energy the trend is reversed, and the maximum dissipation is at the wall.

5. Stability of the secondary flow for $Pr = 0.71$

5.1. *Formulation and numerical method*

The formulation of the stability problem for the stationary transverse cells follows the standard methods of linear stability theory. The Navier–Stokes equations and

the thermal energy balance are written in primitive variables using the Boussinesq approximation. Each of the primitive variables is then written as a sum:

$$q(x, y, z, t) = q_{\rm b}(x) + q_{\rm s}(x, y) + \epsilon q_{\rm p}(x, y, z, t), \tag{30}$$

where subscripts b, s, and p represent the base flow, the secondary flow, and the perturbation, respectively. The equations governing the steady two-dimensional multicellular flow are next subtracted from the general equations so that, after neglecting all terms of order ϵ^2, the remaining system of linear equations for the perturbations governs the stability of the multicellular flow. The final form of these equations is

$$\frac{\partial u}{\partial x} + \frac{\partial v}{\partial y} + \frac{\partial w}{\partial z} = 0, \tag{31}$$

$$\frac{\partial u}{\partial t} + Gr\left[u\frac{\partial u_{\rm s}}{\partial x} + v\frac{\partial u_{\rm s}}{\partial y}\right] + \mathscr{L}u + Gr\frac{\partial p}{\partial x} = 0, \tag{32}$$

$$\frac{\partial v}{\partial t} + Gr\left[u\left(\frac{{\rm d}v_{\rm b}}{{\rm d}x} + \frac{\partial v_{\rm s}}{\partial x}\right) + v\frac{\partial v_{\rm s}}{\partial y}\right] + \mathscr{L}v - T + Gr\frac{\partial p}{\partial y} = 0, \tag{33}$$

$$\frac{\partial w}{\partial t} + \mathscr{L}w + Gr\frac{\partial p}{\partial z} = 0, \tag{34}$$

$$Pr\frac{\partial T}{\partial t} + Gr\,Pr\left[u\left(\frac{\partial T_{\rm b}}{\partial x} + \frac{\partial T_{\rm s}}{\partial x}\right) + v\frac{\partial T_{\rm s}}{\partial y}\right] + \mathscr{L}_T\,T = 0, \tag{35}$$

where the two operators appearing in the equations are defined as

$$\mathscr{L} \equiv -\nabla^2 + Gr\left[u_{\rm s}\frac{\partial}{\partial x} + (v_{\rm b} + {\rm v}_{\rm s})\frac{\partial}{\partial y}\right], \tag{36}$$

$$\mathscr{L}_T \equiv -\nabla^2 + Gr\,Pr\left[u_{\rm s}\frac{\partial}{\partial x} + (v_{\rm b} + v_{\rm s})\frac{\partial}{\partial y}\right], \tag{37}$$

and the subscript p has been dropped. The boundary conditions to be satisfied are

$$u = v = w = T = 0 \quad {\rm at} \quad x = -\tfrac{1}{2}\,{\rm and}\,\tfrac{1}{2}. \tag{38}$$

Since the equations are linear and homogeneous, and do not depend explicitly on z and t, one can assume for the solution an exponential dependency on these two independent variables. The resulting system has one additional feature not present in the analysis of the stability of the base flow; namely, the equations contain coefficients that are periodic functions of y. This type of equation is handled by the Floquet theory (Bender & Orszag 1978) which allows the variables characterizing the perturbations to be written as

$$q(x, y, z, t) = {\rm e}^{{\rm i}dy}\phi(x, y, z, t), \tag{39}$$

where ϕ is a periodic function of y with the original period of the secondary flow, and d is the Floquet exponent. As a result the perturbations can be expanded as

$$q(x, y, z, t) = \sum_{n=-\infty}^{\infty} \phi_n(x)\,{\rm e}^{{\rm i}\varkappa ny + {\rm i}dy + {\rm i}bz + \sigma t}. \tag{40}$$

Substituting the forms given by (40) into the set (31)–(37) leads to an infinite set

of differential equations with homogeneous boundary conditions. These equations then constitute an eigenvalue problem for σ.

Numerical results for the eigenvalue problem are sensitive to the truncation level taken for both x and y. The Chebyshev collocation method is used for the x-dependency. The truncation level in y of the perturbations themselves is of less importance if the y-dependency of the secondary flow is adequately resolved. The secondary flow was calculated with 17 modes in x and 16 in y. Of these, 17 modes in x and 5 modes in y were used to represent the secondary flow in the stability calculations. The perturbations were represented with 17 modes in x and 3 modes in y. The resulting algebraic eigenvalue problem was solved by a complex QR algorithm.

The computational procedure is to first compute a steady nonlinear solution for a particular Gr–α combination, and then to test its stability for three-dimensional disturbances. Previous results, knowledge of the mechanism operating in a particular range of parameters, and interpolation between eigenvalues of sufficiently small real parts were all used in reducing the effort required to determine the onset of secondary instabilities. In a restricted Gr–α parameter space 40 stable nonlinear states were computed and their linear stability was tested to arrive at the results presented in the following section.

As the results are extremely error sensitive, three separate tests were used. First, the stability of the base flow was determined by setting the secondary flow variables to zero. The eigenvalues so calculated were identical to previous values obtained by us and others.

The computer code was also checked by repeating some of the secondary instability calculations of Nagata & Busse (1983) at $Pr = 0$. This was done for the monotone, oscillatory, and Eckhaus instabilities for the parameters quoted by them. The tests were performed with the $17 \times 5 \times 3$ mode resolution. For the monotone instability, the lower bound for the stability limit is about 8200. At $Gr = 8300$, $\alpha = 2.60$, $d = 1.3$, $b = 1.55$ the eigenvalue with the maximum real part is $\sigma_{\max} = (0.77, \approx 10^{-7})$, which is sufficiently close to the value given by Nagata & Busse. For the oscillatory instability, the lower bound for the stability is about 8450. At $Gr = 8500$, $\alpha = 2.60$, $d = 0$, $b = 1.6$, we find $\sigma_{\max} = (0.16, 14.53)$ which again is in accordance with their results. Finally, the growth rates of the Eckhaus instability for the state $Gr = 8500$, $\alpha = 2.60$, $b = 0$ were calculated as functions of d. This state should be stable, with a maximum decay rate at $d = \frac{1}{2}\alpha$. For this test good agreement was again found with the results of Nagata & Busse.

A third test involved a convergence study to ascertain that the spatial resolution is sufficient. Table 1 lists results for two supercritical states with a monotone instability. The first case is at $Gr = 10000$ and $Pr = 0.71$ and is strongly unstable. Results show that for $N_y = 5$, where N_y refers to the number of Fourier modes in the representation of the secondary flow, there is relatively small fractional change when N_x is changed from 17 to 9. The results do not change much when $N_y = 3$, but when the mean flow alone ($N_y = 1$) is used to approximate the secondary flow, the results are seriously in error, with the critical eigenvalue not even having the correct sign. This test was repeated for $Gr = 8500$, which is near the onset of the monotone instability. These results are also given in table 1, and show that $N_y = 5$ and $N_x > 13$ give a reasonably accurate determination of the critical eigenvalue.

From this comparison it is obvious that, at least for our case, using the mean flow alone is completely unacceptable for the computations of secondary instabilities,

N_x	N_y	σ_r	σ_i
		State I	
17	5	12.48	-0.7351×10^{-6}
13	5	12.47	-0.7197×10^{-6}
9	5	12.03	-0.150×10^{-6}
17	3	12.78	-0.3345×10^{-6}
13	3	12.76	-0.5213×10^{-7}
9	3	12.28	-0.2129×10^{-6}
17	1	-19.04	-0.2875×10^{-7}
		State II	
17	5	0.1974	-0.1470×10^{-5}
15	5	0.1969	-0.8441×10^{-6}
13	5	0.1881	-0.1123×10^{-5}
11	5	0.08495	-0.9272×10^{-6}
9	5	0.1368	-0.1061×10^{-6}
7	5	8.9250	-0.2648×10^{-4}
17	3	0.3101	-0.1649×10^{-5}
13	3	0.3007	-0.1275×10^{-5}
9	3	0.2341	-0.1045×10^{-5}
17	1	-22.220	-0.7212×10^{-5}

TABLE 1. Convergence study of the secondary stability code for air. State I: $Gr = 10000$, $\alpha = 2.81$, $d = 1.3$, $b = 1.6$; State II: $Gr = 8500$, $\alpha = 2.81$, $d = 1.3$, $b = 1.6$

even if the nonlinear state is well-resolved. Whereas the numerical appeal to do so is great (as one may use a modified base flow stability code alone), the results do not justify such an approach. Studies with $N_y = 3$ (or $N_y = 2$ when the mean perturbation is zero) have been reported by Herbert (1983) and Orszag & Patera (1983). In the latter study the secondary stability results have been compared to direct simulations of the three-dimensional equations using a nonlinear initial-value code. This approach as noted above is a good way to cross-check the numerical results.

5.2. Secondary stability results

In figure 11 the results of the investigation of the secondary instabilities of the stable transverse rolls are summarized. Grashof number was varied in the range $8037 < Gr < 10000$, the lower value being the critical Grashof number from linear stability theory of the base flow. States with wavenumbers in the range $1.9 < \alpha < 3.4$ were examined, the critical wavenumber of the base flow instabilities being $\alpha = 2.81$. Shown in the figure are curves from three instability mechanisms which constrain the domain of the stable cells. These are two types of the monotone instabilities and the Eckhaus instability. In addition, the stability curve for an oscillatory mode is shown, even though it plays no direct role in the loss of stability of the secondary cells.

5.2.1. The Eckhaus instability

The Eckhaus instability operates as a two-dimensional mechanism by limiting the lower and upper stable wavenumbers (see Drazin & Reid 1981, pp. 416–420). Thus at any given Grashof number, the Eckhaus instability curve is contained within the linear stability curve. From figure 11 it is seen that, in our case, the Eckhaus curve is more non-symmetric about the critical wavenumber, with the longer waves being more stable, than in the study by Nagata & Busse (1983). This observation suggests
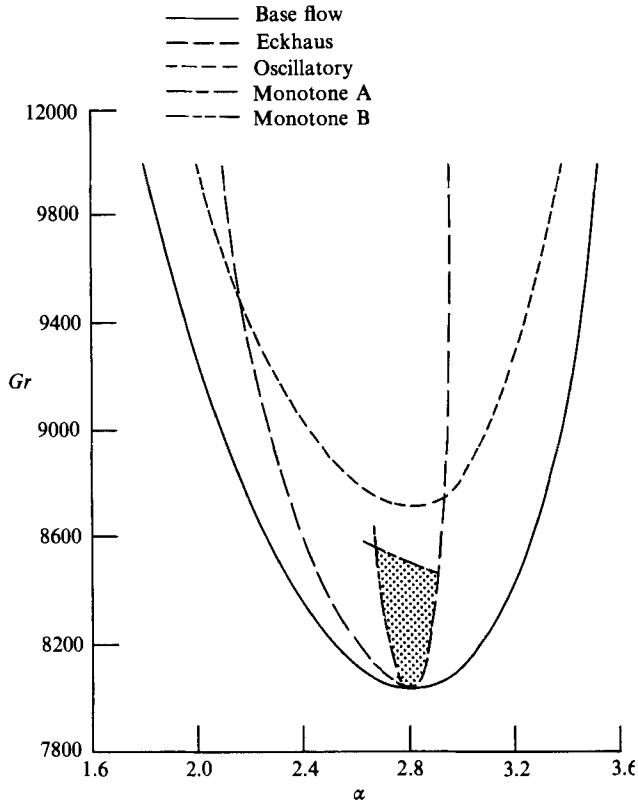
FIGURE 11. Stability map of the multicellular flow for air ($Pr = 0.71$). The shaded area represents the domain of stable two-dimensional cells.

that the most stable transverse cells in a vertical cavity have a longer wavelength than those at the critical state. The tendency towards longer wavelengths is consistent with weakly nonlinear theory and has been reported by Lee & Korpela (1983) in a cavity of finite, but large, aspect ratio. The right branch of the Eckhaus curve rises steeply and shows that cells with $\alpha > 2.95$ are unstable.

The growth rate of the Eckhaus instability as a function of d and for various values of α is shown in figure 12. The curves are similar to those calculated by Nagata & Busse for $Pr = 0$. The abscissa in figure 12 is normalized by α, so easy comparison between different values of α is possible. A characteristic property of the curves is a minimum at $d/\alpha \approx \frac{1}{2}$, showing that the principal parametric subharmonic mode is not the preferred one. This is in accordance with the findings of Nagata & Busse who mention that the examination of only subharmonic modes by Pierrehumbert & Widnall (1982) is insufficient. It is also seen from the curves that there exists a well-defined trend of preferred wavenumber ranges that are first amplified. The first unstable subharmonic for α to the right of the Eckhaus curve starts with values of $d/\alpha \approx 1$ and diminishes away from the Eckhaus curve. Conversely, for values of α to the left of the curve, the first unstable subharmonic has a very small wavenumber. Nagata & Busse found relatively symmetrical results about $d/\alpha = \frac{1}{2}$. The lack of symmetry in figure 12 must be attributed to the departure from the $Pr = 0$ limit. The usual identification of the modes of instability as either 'shear' or 'buoyancy' driven which prevails for the base flow instability case does not neccessarily hold true for
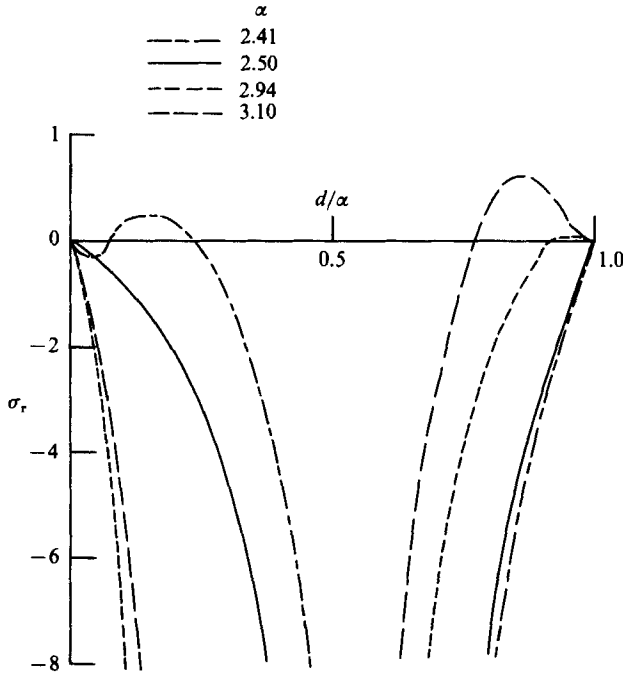
FIGURE 12. Growth rates of Eckhaus instability for several values of α ($Pr = 0.71$, $Gr = 8500$).

the secondary instability. Small and intricate differences between seemingly similar parameters may lead to different dominating instability mechanisms. Therefore, it is not surprising to find differences between our observations and those of Nagata & Busse, including those that show up for the Eckhaus instability.

5.2.2. The monotone instabilities

The two modes of monotone instability shown in figure 11, are designated as monotone A and B modes. The monotone A instability constraints the domain of the stable vortices from above, and is apparently the same monotone instability as found by Nagata & Busse. The resulting flow is three-dimensional because both b and d have finite values for the critical mode. For all the states considered the value of d was slightly less or nearly equal to $\frac{1}{2}\alpha$. The deviation from $d = \frac{1}{2}\alpha$ may lie in the lack of perfect periodicity of the results. The departure from perfect periodicity is likely to have been caused by slightly inadequate y-resolution of the secondary flow representation. In the limit of an infinite number of modes the flow is expected to be perfectly periodic in y. Lack of perfect periodicity was also noted by Nagata & Busse, whose numerical methods are more efficient for the inclusion of more Fourier modes in the secondary flow. The computed values of d vary at most by about 7% from $d = \frac{1}{2}\alpha$. The value of b at the critical states does not vary greatly with α, being about 1.6 for the values of α tested. Nagata & Busse obtained for $Pr = 0$ a value between 1.5 and 1.6 when $\alpha = 2.6$. Thus the monotone instability leads to a three-dimensional tertiary flow with twice the wavelength of the secondary flow, and it was discovered by Nagata & Busse that the flow is one in which pairing of adjacent cells takes place.

The stability curve for the monotone B mode is also shown in figure 11. To the left

of this curve the secondary flow is unstable; to the right it is stable. The curve originates from the vicinity of the critical state of the base flow ($Gr_c = 8037$, $\alpha_c = 2.81$) and limits the minimum allowable stable wavenumber to about $\alpha = 2.68$ at $Gr = 8550$. A characteristic property of monotone B instability is that it exhibits, as a function of α, a rather wide region of growth rates of nearly the same magnitude. Near the stability curve both b and d are very small. They assume values of at most $d = 0.4$ and $b = 0.6$ for states further away from the stability curve, in the range of parameters tested (up to $Gr = 9000$). Thus the characteristic wavelength associated with the three-dimensional monotone B instability is much larger than the original secondary flow wavelength.

The monotone B instability was found to resemble in many ways the skewed varicose instability in Rayleigh–Bénard convection. The skewed varicose instability for Rayleigh–Bénard convection operates at the low to moderate Prandtl-number range only. At the limit of stability, the values of both d and b vanish, and therefore the skewed varicose instability goes over to a translational instability of neutral type. At finite values of b and d, the skewed varicose instability distorts the rolls in the spanwise direction such that periodic thinning and thickening of the cells is noticeable, giving the pattern a skewed appearance.

Owing to the different base flow in the case considered here, the appearance of the cellular structure now may be quite different from in Rayleigh–Bénard convection. In addition, whereas the skewed varicose instability is the most important mechanism constraining the upper limit of the wavenumber range for Rayleigh–Bénard convection in the low to moderate Prandtl-number range, the results shown here produce exactly the opposite effect. In figure 11 the monotone B instability is seen to constrain the lower limit of the stable wavenumbers. This difference is not unexpected, because transverse cells may lead to a different dependency on the primary wavenumber than the longitudinal rolls in Rayleigh–Bénard flow. The skewed varicose mechanism is the only mode of instability for Rayleigh–Bénard convection known to both change the original cell wavelength and to introduce a periodic pattern in the y-direction. This feature is present in the monotone B instability.

One might wonder why the monotone A or B instabilities are not generally observed in laboratory experiments. There may be several reasons for this. First, most flow visualization studies of the transverse convection cells involve using a light sheet which cuts through a vertical (x, y)-plane, the sidewalls being made of highly conducting material such as copper or aluminium to keep their temperatures constant. Thus the spanwise structure is impossible to see in such an experiment. The second reason concerns the finite aspect ratios in laboratory experiments. The finite aspect ratio may alter the flow through the imposed thermal stratification, as well as by introducing additional geometrical constraints. The thermal stratification both delays the appearance of the multicellular flow and may have some effects on the growth of the finite-amplitude flow. Also, for monotone B instability it is noted that the values of b and d of the developing tertiary motions are very small; they are vanishingly small near its stability curve. This property implies very large wavelengths in both the vertical and spanwise directions. It is noted that since the monotone A instability constrains the domain of the stable cells from above, it is most likely to be seen as the Grashof number is increased. To resolve, say, 20 cells in this case, a cavity with an aspect ratio of about 100 is sufficient.
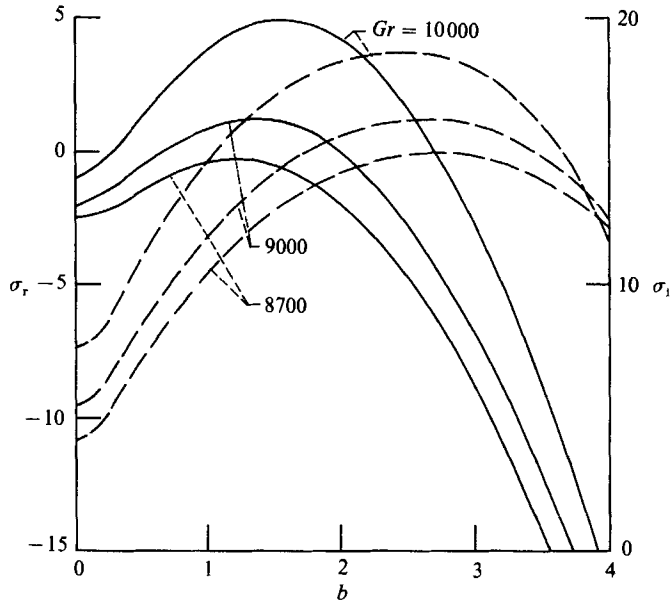
FIGURE 13. Real (———) and imaginary (- - - -) parts of the critical eigenvalue at several Grashof numbers for the oscillatory instability ($Pr = 0.71$, $\alpha = 2.81$).

5.2.3. The oscillatory instability

The oscillatory instability shown by the short dashed line in figure 11 has the same features as that found by Nagata & Busse for $Pr = 0$. The maximum growth rate corresponds to $d = 0$, $b \approx 1.4$–1.6. Figure 13 shows the real and imaginary parts of the oscillatory instability for several Grashof numbers at $\alpha = 2.81$. The critical eigenvalue always appears as a pair of complex conjugates. This result is different from the analyses of both Nagata & Busse (1983) and Pierrehumbert & Widnall (1927). Nagata & Busse found two real eigenvalues which join to form a pair of complex conjugates, and Pierrehumbert & Widnall found two imaginary eigenvalues which join to form a pair of complex conjugates as b increases. However, since their study was limited to the inviscid case only, the real parts of their eigenvalues are identically zero, which complicates the analysis of the b-dependency. Nagata & Busse show the total stream pattern for the $Pr = 0$ case. From this it can be concluded that when the flow is viewed in the (x, y)-plane, the cells are seen to move periodically up and down. In the (y, z)-plane the flow appears as a pair of travelling waves which bend the rolls periodically.

6. Discussion

The topics investigated in this study were chosen with the aim of acquiring a general understanding of the flow characteristics and stability of the multicellular flow of natural convection in a vertical cavity.

An examination of the flow from both the, traditionally separate, spectral and physical views is central to the understanding of the overall transfer processes. Physical description of the flow clearly shows the interdependency between the temperature and flow fields. In a time-dependent high-Prandtl-number flow, the causality between the two fields becomes apparent when quantities such as the

secondary fields and the buoyant production are examined. The results here suggest that temperature fluctuations originate near the 'critical layers' and are convected along the two vertical sides of the cavity. These fluctuations directly contribute to the dominant buoyant production of kinetic energy during one part of the cycle. The data also suggest that there are small changes in the temperature field during the cycle, but that large effects are noted for the secondary velocity fields. The process can be likened to an oscillator with damping, in which the forcing function is altered by the motion such a way as to sustain a stable oscillation. It could not be compared, however, to an oscillator in which energy is simply being transferred between the kinetic and the potential energy fields, for dissipation results in a large reduction in the kinetic energy in one part of the cycle which is being replenished during the other half.

A spectral examination of these flows revealed several additional aspects. The kinetic energy and thermal variance spectra were found to be smooth and the logarithms of either quantity varied linearly with the wavenumber. This behaviour resembles the one-dimensional kinetic energy spectrum of Taylor–Couette flow, which is purely hydrodynamic. Therefore for a relatively low-Pr fluid (air), the buoyant production effects were still small in comparison with the triad interaction term in supplying the kinetic energy of the disturbances. The same spectra for oil show that the oscillations in the flow are restricted to only the first four modes, and that the role of the rest of the spectra is simply to dissipate the kinetic energy and thermal variance.

The secondary stability map produced for air in a vertical slot shows a rather small region of stable cells. This region is confined by the Eckhaus and monotone instabilities as in the flow of a fluid with $Pr = 0$, and another instability resembling (except, perhaps, for its physical appearance) the skew varicose instability in Rayleigh–Bénard convection. The two-dimensional cells in air are stable only for $Gr \leqslant 8560$, a limit that must be observed in two-dimensional simulations of the flow. There seems to be little reason for computing two-dimensional flows with higher and higher Grashof numbers.

REFERENCES

BENDER, C. M. & ORSZAG, S. A. 1978 *Advanced Mathematical Methods for Scientists and Engineers.* McGraw-Hill.

BERGHOLZ, R. F. 1978 Instabilities of steady natural convection in a vertical fluid layer. *J. Fluid Mech.* **84**, 743.

BOLTON, E. W., BUSSE, F. H. & CLEVER, R. M. 1986 Oscillatory instabilities of convection rolls at intermediate Prandtl numbers. *J. Fluid Mech.* **164**, 469–485.

BUSSE, F. H. 1981 Transition to turbulence in Rayleigh–Bénard convection. In *Hydrodynamic Instabilities and the Transition to Turbulence* (ed. H. L. Swinney & J. P. Gollub), pp. 99–137. Springer.

DRAZIN, P. G. & REID, W. H. 1981 *Hydrodynamic Instability.* Cambridge University Press.

GERSHUNI, G. Z. & ZHUKHOVITSKII, E. M. 1976 Convective instability of incompressible fluid. US Department of Commerce.

GILL, A. E. & DAVEY, A. 1969 Instabilities of a buoyancy-driven system *J. Fluid Mech.* **35**, 775–798.

GOTTLIEB, D. & ORSZAG, S. A. 1977 *Numerical Analysis of Spectra Methods: Theory and Applications.* SIAM.

HERBERT, T. 1983 Secondary instability of plane channel flow to subharmonic three-dimensional disturbances. *Phys. Fluids* **26**, 871–874.

HOLLANDS, K. G. T. & KONICEK, L. 1973 Experimental study of the stability of differentially heated inclined air layers. *Int. J. Heat Mass Transfer* **16**, 1467.

KORPELA, S. A., GOZUM, D. & BAXI, C. B. 1973 On the stability of the conduction regime of natural convection in a vertical slot. *Intl J. Heat Mass Transfer* **2**, 193.

KUO, H. P. 1986 Stability and finite amplitude natural convection in a shallow cavity with horizontal heating. Ph.D. dissertation, The Ohio State University.

LAURIAT, G. & GESRAYAUD, G. 1985a Natural convection in air-filled cavities of high aspect ratios: discrepancies between experimental and theoretical results. *ASME* 85-HT-37.

LAURIAT, G. & DESRAYAUD, G. 1985b Influences of the boundary conditions and linearization on the stability of a radiating fluid in a vertical layer. *Intl J. Heat Mass Transfer* **28**, 1613–1617.

LEE, Y. & KORPELA, S. A. 1983 Multicellular natural convection in a vertical slot. *J. Fluid Mech.* **126**, 91–121.

MARCUS, P. S. 1984a Simulation of Taylor–Couette flow. Part 1. Numerical methods and comparison with experiments. *J. Fluid Mech.* **146**, 45–64.

MARCUS, P. S. 1984b Simulation of Taylor–Couette flow. Part 2. Numerical results for wavy-vortex flow with one travelling wave. *J. Fluid Mech.* **146**, 65–113.

NAGATA, M. & BUSSE, F. H. 1983 Three-dimensional tertiary motions in a plane shear layer. *J. Fluid Mech.* **135**, 1–26.

ORSZAG, S. A. & PATERA, A. T. 1983 Secondary instability of wall bounded shear flows. *J. Fluid Mech.* **128**, 347–385.

PIERREHUMBERT, R. T. & WIDNALL, S. E. 1982 The two- and three-dimensional instabilities of a spatially periodic shear layer. *J. Fluid Mech.* **114**, 59–82.

PRANDTL, L. 1953 *The Essentials of Fluid Mechanics.* NY: Hafner.

SCHINKEL, W. M. W. 1980 Natural convection in inclined air-filled cavities. Ph.D. dissertation, Dept. of Applied Physics, Delft University.

VEST, C. M. & ARPACI, V. S. 1969 Stability of natural convection in a vertical slot. *J. Fluid Mech.* **36**, 1–15.